Table 2. CFOV sensitivity of microPET II for different coincidence timing windows. The energy window is 250 to 750 keV.

Timing window (ns)	Sensitivity (%)
2	0.96
6	2.07
10	2.29
14	2.31
18	2.31

Table 3. Scatter fraction (SF) for mouse-sized and rat-sized phantoms.

Phantom	Energy window	SF (%)
25 mm $\phi \times$ 70 mm (34 cc)	150–750 keV	12.8
	250–750 keV	9.7
	350–750 keV	7.2
	450–750 keV	5.3
60 mm $\phi \times$ 150 mm (424 cc)	150–750 keV	53.7
	250–750 keV	45.6
	350–750 keV	35.9
	450–750 keV	23.3

5.3. Scatter fraction

Table 3 shows the scatter fraction as a function of lower energy threshold for the mouse-sized phantom and the rat-sized phantom. As expected, the scatter fraction increases as the phantom volume increases and as the lower energy threshold decreases. These scatter fractions are consistent with those measured previously for small-animal systems and show that for a rat-sized object, the scatter fraction can be very significant (20–50%). These measured scatter fraction values are used to calculate the NEC rates presented in the next section.

5.4. Count-rate performance

Figure 4 shows total (prompt) counting rates, random counting rates and the calculated NEC curves from the mouse-sized phantom for different energy and timing windows. The peak total counting rates were around 700 000 cps at which point saturation is clearly seen (discontinuity in the curves). The activity at which saturation occurs depends strongly on the energy and timing window, and occurs as low as 2.4 MBq cc^{-1} (corresponding to 82 MBq of activity in the cylinder) for a 150–750 keV energy window and a 14 ns timing window. The increase in randoms counting rate with activity depends more strongly on the lower energy threshold than the timing window. For the mouse-sized phantom, the best NEC performance across the entire range of typical injected doses is to use an energy window of 150–750 keV and a timing window of 10 ns. For these settings, the NEC curve peaks at 235 000 cps at an activity concentration of around 2.35 MBq cc^{-1} ($\sim$80 MBq in the phantom). This wide-open energy window maximizes sensitivity, and because the scatter fraction for mouse imaging is low, the increase in sensitivity outweighs the increase in scatter. The timing window can also be left wide open (even for a 14 ns window, the NECs are only reduced slightly towards the top of the injected dose range), because there is only a small amount of activity outside the field of view, and therefore the coincidence to singles ratio is quite favourable. Generally, for mouse imaging, NEC rates achieved will be limited by the injected dose that is administered

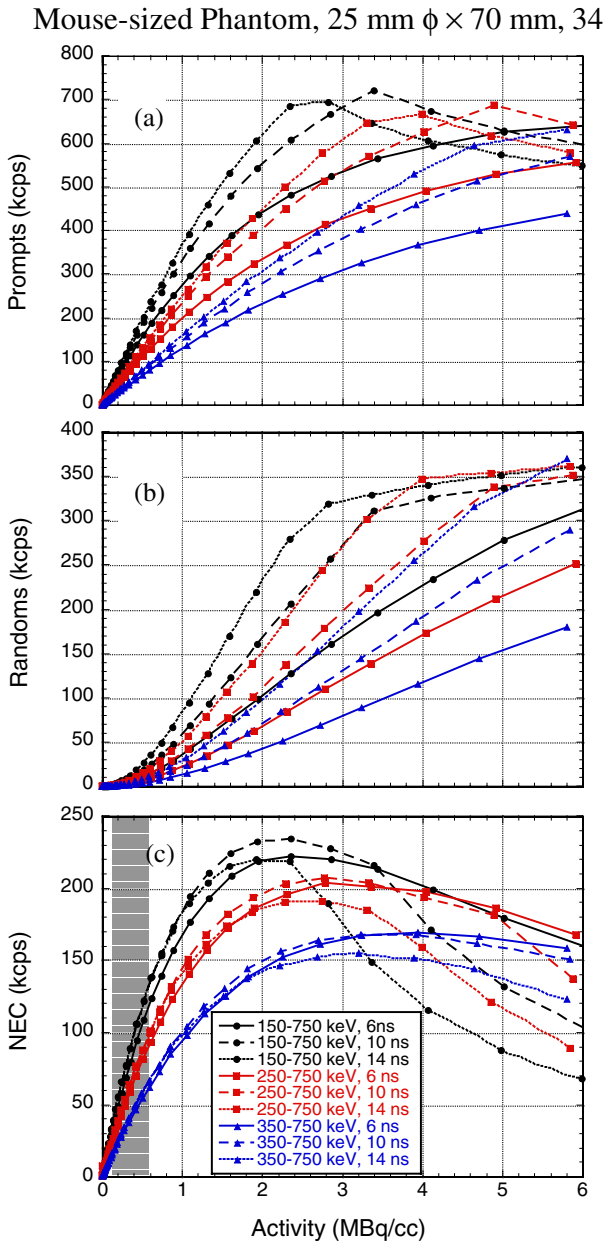

Figure 4. Prompt coincidence (a), random (b) and NEC (c) counting rates of microPET II for a mouse-sized phantom for different energy and timing windows. Shaded area in (c) indicates the typical injected dose range for mouse studies.

(typically in the range 3.7–37 MBq, limited by the volume of the injectate, specific activity of the radiopharmaceutical, and by concerns regarding mass effects) and not by count-rate limitations of the scanner.

Figure 5 shows the total counting rate, random counting rate and NEC curves for the rat-sized phantom. Different trends are observed, primarily due to an increase in random coincidence events and scattered events because much of the phantom extends beyond the

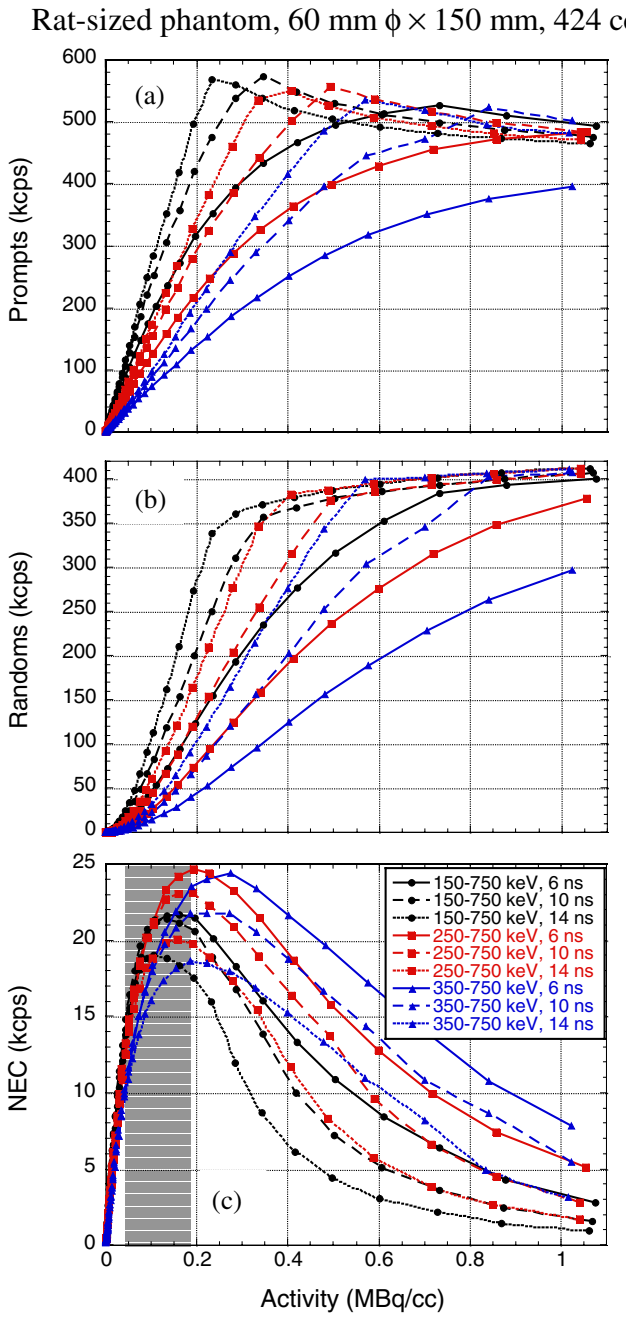

Figure 5. Prompt coincidence (a), random (b) and NEC (c) counting rates of microPET II for a rat-sized phantom for different energy and timing windows. Shaded area in (c) indicates the typical injected dose range for rat studies.

axial FOV of the scanner in a region that is difficult to shield, and because the volume of the phantom is more than a factor of 10 larger. The peak total counting rate is reduced to about 550 kcps due to the larger number of random coincidences. The peak NEC counting rate of 24 600 cps is achieved at an activity concentration of 0.19 MBq cc^{-1} (∼80 MBq in phantom)

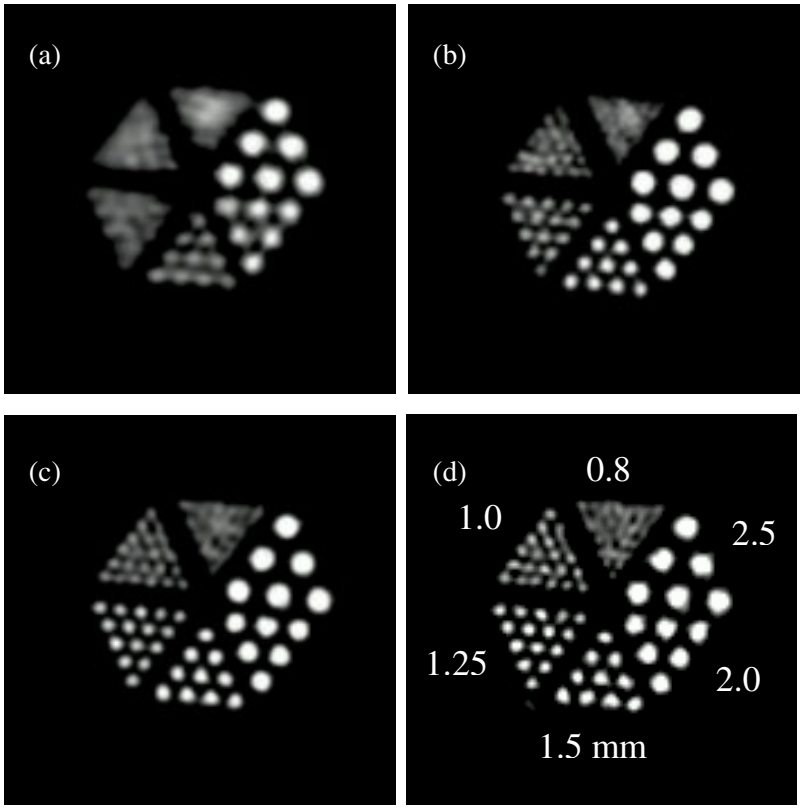

Figure 6. Images of a miniature Derenzo hot-rod phantom. The rod diameters are shown in (d). The centre-to-centre separations are twice the rod diameter. The phantom was filled with 22 MBq (0.6 mCi) $^{18}F^{-}$ and scanned for 60 min. (a) Image measured by Concorde P4 scanner and reconstructed by FBP. (b) Image measured by microPET II and reconstructed by FBP. (c) Image measured by microPET II and reconstructed by MAP with β of 0.1. (d) Image measured by microPET II and reconstructed by MAP with β of 0.01.

with an energy window of 250–750 keV, and a timing window of 6 ns. Notably, the optimal energy and timing windows vary across the range of typical injected doses. For example, at low doses (concentrations <0.1 MBq cc^{-1}, activity 'injected' in phantom <42 MBq), the 150–750 keV energy window and 10 ns timing window provide the best NEC performance. At higher doses (concentrations of between 0.1 and 0.24 MBq cc^{-1}, corresponding to 'injected' activities of between 42 and 100 MBq) a 250–750 keV energy window and 6 ns timing window provide the highest NEC rate. It is also clear that for rat imaging, NEC performance is being impacted by system count-rate limitations for injected doses towards the high end of the range. However, it should be noted that all these studies were conducted with no attempt to shield out of FOV activity.

6. Imaging studies: results

6.1. Derenzo phantoms

Figure 6 shows a transverse slice of the miniature Derenzo hot-rod phantom reconstructed from data taken on the Concorde P4 microPET scanner and on the microPET II scanner for

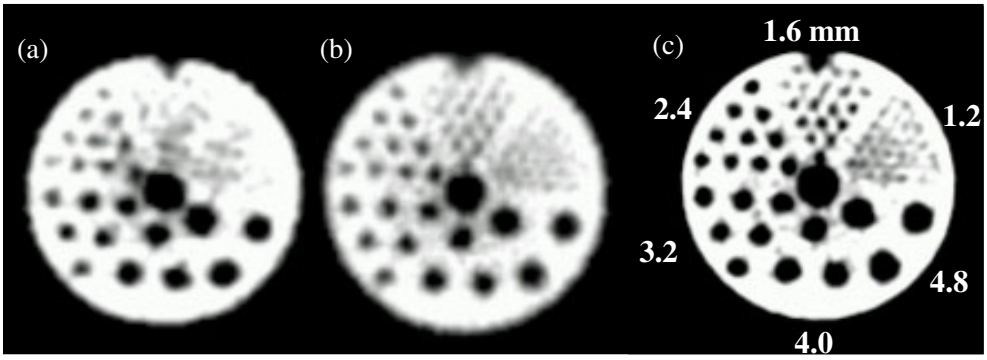

Figure 7. Images of a miniature Derenzo cold-rod phantom. The rod diameters are shown in (c). The centre-to-centre separations are twice the rod diameter. The phantom was filled with 37 MBq (1 mCi) $^{18}F^{-}$, and scanned for 60 min. (a) Image measured by Concorde P4 and reconstructed by FBP. (b) Image measured by microPET II and reconstructed by FBP. (c) Image measured by microPET II and reconstructed by MAP with β of 0.4.

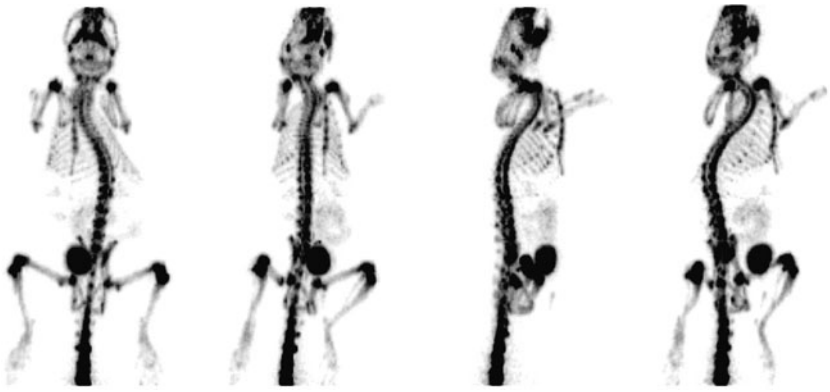

Figure 8. Projection views of bone scan of a 31 g mouse injected with 37 MBq (1 mCi) of $^{18}F^{-}$, scanned across two bed positions at 60 min per bed position, starting 180 min after injection. Image reconstructed by MAP with β equal to 0 (MLEM).

different reconstruction algorithms. Using FBP reconstruction, the Concorde P4 microPET® system can resolve the 1.5 mm diameter rods, and the microPET II system can resolve rods that are 1.25 mm in diameter. Using MAP reconstruction, rods as small as 1 mm diameter can be easily resolved with the microPET II system. Figure 7 shows a transverse slice through the miniature Derenzo cold-rod phantom. The cold-rod phantom is a much more difficult object to image as it provides an evaluation of both resolution and contrast. With the Concorde P4 microPET, the smallest rods that are clearly resolved with FBP reconstruction are the 2.4 mm rods. With microPET II, rods as small as 1.6 mm can be resolved, and with MAP reconstruction ($\beta = 0.4$, corresponding to a volumetric resolution of 1.5 μl at CFOV), it is possible to resolve some of the 1.2 mm rods.

6.2. Bone metabolism: mouse and rat whole-body imaging

Figures 8 and 9 show maximum intensity projection views of $^{18}F^{-}$ bone images of a mouse and a rat respectively. The individual ribs of the mouse and rat can be clearly identified, even

Figure 9. Maximum intensity projection views of bone scan of a 304 g rat injected with 107 MBq (2.9 mCi) of $^{18}F^{-}$, scanned across five bed positions at 20 min per bed position, starting 210 min after injection. Image reconstructed by MAP with β equal to 0 (MLEM).

though no cardiac or respiratory gating was employed. Increased $^{18}F^{-}$ uptake is apparent in the growth plates of the bones (especially visible in the wrist and joints in the limbs) indicating, unlike humans, that there is continued growth of the bones in rodents into adulthood. These studies show the potential of microPET II for imaging high contrast objects, where the full resolving power of the instrument can clearly be appreciated.

6.3. Glucose utilization: mouse and rat brain

Figures 10 and 11 show coronal sections through FDG images of the mouse and rat brain. Images are reconstructed with a β value of 0.4 which corresponds to a volumetric resolution of approximately 1.5 μl at CFOV. In the rat, enhanced uptake is evident in the cortex, thalamus and striatum. There also is uptake in many extracerebral areas, including muscle, harderian glands and salivary glands. In the mouse, due to the small width of the white matter tracts, visualization of major brain structures is still limited, even though the brain covers many resolution elements (mouse brain is approximately 450 mm^3 $\approx$ 450 resolution elements). However, the resolution should be sufficient for quantifying activity in major brain structures, assuming the structures can be located through the use of a stereotactic head-holder and/or registration to a mouse brain atlas.

6.4. Glucose utilization: mouse and rat heart

Figures 12 and 13 show transverse, coronal and sagittal views of FDG heart images of a mouse and a rat. No cardiac gating was applied in these studies. The two heart chambers can be clearly identified with particularly clear demarcation of the left ventricular wall, even in the mouse where the diameter of the left ventricle is only around 6 mm. Once again, in this high contrast scenario, the resolution of the scanner can be clearly appreciated.

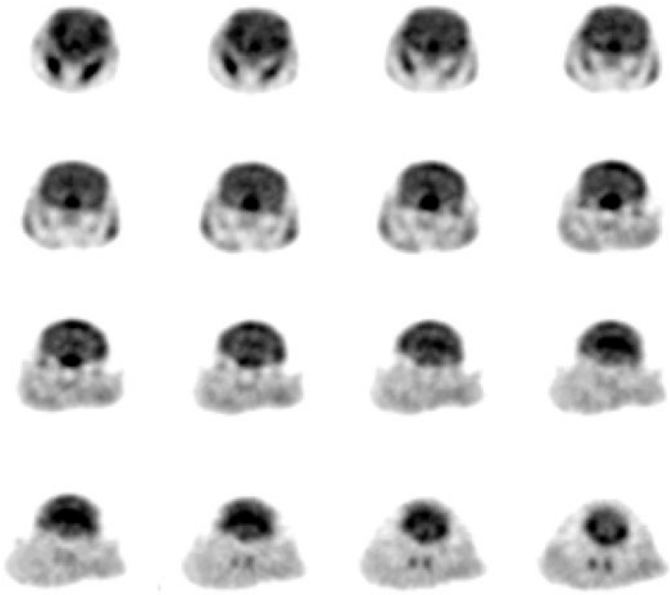

Figure 10. Transverse slices from brain image of a 32 g mouse injected with 21 MBq (0.58 mCi) of ^{18}FDG, scanned for 60 min, starting 40 min after injection. Image reconstructed by MAP with β equal to 0.4.

Figure 11. Transverse slices from brain of a 309 g rat injected with 31 MBq (0.84 mCi) of ^{18}FDG, scanned for 60 min, starting 60 min after injection. Image reconstructed by MAP with β equal to 0.4.

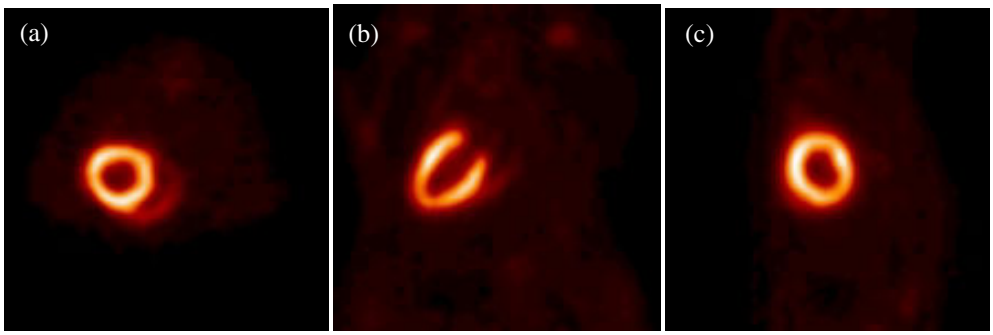

Figure 12. Transverse (a), coronal (b) and sagittal (c) views of heart images of a 32 g mouse injected with 21 MBq (0.58 mCi) of ^{18}FDG, scanned for 60 min, starting 120 min after injection. Image reconstructed by MAP with β equal to 0.1.

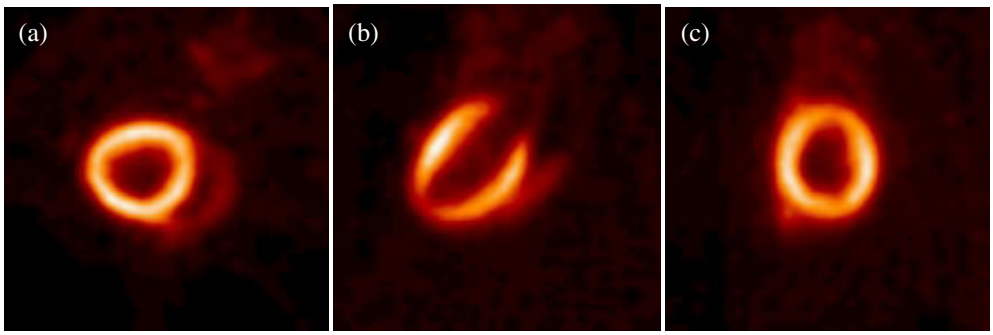

Figure 13. Transverse (a), coronal (b) and sagittal (c) views of heart images of a 300 g rat injected with 81 MBq (2.2 mCi) of ^{18}FDG, scanned for 60 min, starting 40 min after injection. Image reconstructed by MAP with β equal to 0.1.

7. Discussion and conclusion

The microPET II system has now been used in a range of animal studies and has proved very stable over the past year of continuous operation. Our performance evaluation indicates that microPET II meets its design specifications of 1 μl reconstructed resolution for a mouse-sized object when used in conjunction with a MAP reconstruction algorithm that accurately models system geometry and other physical processes that impact the localization of the annihilation photons. The sensitivity is a strong function of the lower energy threshold in the 150–300 keV range, but a very weak function of the upper energy threshold above 650 keV. A timing window of 10 ns is sufficient to include virtually all true coincidence events. The sensitivities at the CFOV are 2.3% and 3.3% for energy windows of 250 to 750 keV and 150 to 750 keV respectively, when the timing window is 10 ns. These represent very significant improvements in both sensitivity and resolution (roughly a factor of 4 in both cases) compared with our first microPET prototype (Cherry *et al* 1997, Chatziioannou *et al* 1999).

The counting-rate performance measurements show that different energy and timing windows should be used to optimize mouse and rat imaging. The peak NEC counts are 235 000 cps and 24 600 cps for a mouse-sized and a rat-sized object, respectively. It should also be noted that the NEC measurements were made with phantoms containing homogeneous activity distributions, which rarely occurs for real animal studies. Furthermore, the NEC

curves are sensitive to the value of the scatter fraction used in equation (3), and the precise methodology for measuring the scatter fraction is open to some debate. Therefore, the NEC data, while useful for guiding optimal settings for timing and energy windows, should not be overinterpreted. Finally, there was no attempt to shield activity outside of the axial field of view and it is likely that incorporating some shielding into the bed design may assist NEC rates, especially in rat studies.

Phantom and animal studies demonstrate the capability of microPET II for small-animal imaging, especially for studies where high spatial resolution is required to resolve small organs or sub-structures within an animal. Future works include further optimization of the MAP reconstruction, development of a component based normalization approach (Bai *et al* 2002, Casey *et al* 1995) and evaluation of quantitative accuracy for *in vivo* studies.

Acknowledgments

The authors thank Evren Asma for assistance with the MAP reconstruction code, and Dr Guido Zavattini, Dr Arion Chatziioannou, Robert Silverman and Jennifer Stickel for useful discussions and technical help. The authors also thank Steven Rendig and Calliandra Harris for their assistance in performing the animal studies. This work was funded by NIH grants R01 EB000561 and R01 EB000363.

References

Bai B, Li Q, Holdsworth C H, Asma E, Tai Y C, Chatziioannou A and Leahy R M 2002 Model-based normalization for iterative 3D PET image reconstruction *Phys. Med. Biol.* **47** 2773–84

Bloomfield P M, Myers R, Hume S P, Spinks T J, Lammertsma A A and Jones T 1997 Three-dimensional performance of a small-diameter positron emission tomograph *Phys. Med. Biol.* **42** 389–400

Budinger T F, Benaron D A and Koretsky A P 1999 Imaging transgenic animals *Annu. Rev. Biomed. Eng.* **1** 611–48

Casey M E, Gadagkar H and Newport D 1995 A component based method for normalization in volume PET *Proc. the 1995 Int. Meeting on Fully Three-Dimensional Image Reconstruction in Radiology and Nuclear Medicine* pp 67–71

Chatziioannou A F, Cherry S R, Shao Y, Silverman R W, Meadors K, Farquhar T H, Pedarsani M and Phelps M E 1999 Performance evaluation of microPET: a high-resolution lutetium oxyorthosilicate PET scanner for animal imaging *J. Nucl. Med.* **40** 1164–75

Chatziioannou A, Qi J, Moore A, Annala A, Nguyen K, Leahy R and Cherry S R 2000 Comparison of 3-D maximum a posteriori and filtered backprojection algorithms for high-resolution animal imaging with microPET *IEEE Trans. Med. Imaging* **19** 507–12

Chatziioannou A, Tai Y C, Doshi N and Cherry S R 2001 Detector development for microPET II: a 1 μl resolution PET scanner for small animal imaging *Phys. Med. Biol.* **46** 2899–910

Cherry S R and Gambhir S S 2001 Use of positron emission tomography in animal research *Inst. Lab. Anim. Res. J.* **42** 219–32

Cherry S R, Shao Y, Siegel S, Silverman R W, Mumcuoglu E, Meadors K and Phelps M E 1996 Optical fiber readout of scintillator arrays using a multi-channel PMT: a high resolution PET detector for animal imaging *IEEE Trans. Nucl. Sci.* **43** 1932–7

Cherry S R *et al* 1997 MicroPET: a high resolution PET scanner for imaging small animals *IEEE Trans. Nucl. Sci.* **44** 1161–6

Correia J A, Burnham C A, Kaufman D and Fischman A J 1999 Development of a small animal PET imaging device with resolution approaching 1 mm *IEEE Trans. Nucl. Sci.* **46** 631–5

Defrise M, Kinahan P E, Townsend D W, Michel C, Sibomana M and Newport D F 1997 Exact and approximate rebinning algorithms for 3D PET data *IEEE Trans. Med. Imaging* **16** 145–58

Del Guerra A, Di Domenico G, Scandola M and Zavattini G 1998 YAP-PET: first results of a small animal positron emission tomograph based on YAP:Ce finger crystals *IEEE Trans. Nucl. Sci.* **45** 3105–8

Huber J S and Moses W W 1999 Conceptual design of a high-sensitivity small animal PET camera with 4 pi coverage *IEEE Trans. Nucl. Sci.* **46** 498–502

Jeavons A P, Chandler R A and Dettmar C A R 1999 A 3D HIDAC-PET camera with sub-millimetre resolution for imaging small animals *IEEE Trans. Nucl. Sci.* **46** 468–73

Knoess C *et al* 2003 Performance evaluation of the microPET R4 PET scanner for rodents *Eur. J. Nucl. Med. Mol. Imaging* **30** 737–47

Lecomte R, Cadorette J, Rodrigue S, Lapointe D, Rouleau D, Bentourkia M, Yao R and Msaki P 1996 Initial results from Sherbrooke avalanche photodiode positron tomograph *IEEE Trans. Nucl. Sci.* **43** 1952–57

Miyaoka R S, Kohlmyer S G and Lewellen T K 2001 Performance characteristics of micro crystal element (MiCE) detectors *IEEE Trans. Nucl. Sci.* **48** 1403–7

Phelps M E 2000 Inaugural article: positron emission tomography provides molecular imaging of biological processes *Proc. Nat. Acad. Sci. USA* **97** 9226–33

Qi J and Leahy R M 2000 Resolution and noise properties of MAP reconstructions in fully 3D PET *IEEE Trans. Med. Imaging* **19** 493–506

Qi J, Leahy R M, Cherry S R, Chatziioannou A and Farquhar T H 1998 High-resolution 3D Bayesian image reconstruction using the microPET small-animal scanner *Phys. Med. Biol.* **43** 1001–13

Seidel J, Vaquero J J and Green M V 2002 Resolution uniformity and sensitivity of the NIH ATLAS small animal PET scanner: comparison to simulated LSO scanners without depth-of-interaction capability 2001 *IEEE Nuclear Science Symposium Conference Record* vol 3 (Piscataway, NJ: IEEE) pp 1555–8

Shao Y, Silverman R W and Cherry S R 2000 Evaluation of Hamamatsu R5900 series PMTs for readout of high-resolution scintillator arrays *Nucl. Instrum. Methods* A **454** 379–88

Siegel S, Silverman R W, Shao Y and Cherry S R 1996 Simple charge division readouts for imaging scintillator arrays using a multi-channel PMT *IEEE Trans. Nucl. Sci.* **43** 1634–41

Strother S C, Casey M E and Hoffman E J 1990 Measuring PET scanner sensitivity: relating count rates to image signal-to-noise ratios using noise equivalent counts *IEEE Trans. Nucl. Sci.* **37** 783–8

Tai Y C, Chatziioannou A, Siegel S, Young J, Newport D, Goble R N, Nutt R E and Cherry S R 2001 Performance evaluation of the microPET P4: a PET system dedicated to animal imaging *Phys. Med. Biol.* **46** 1845–62

Tai Y C, Chatziioannou A, Yang Y F, Silverman R W, Meadors K, Siegel S, Newport D, Stickel J R and Cherry S R 2003 MicroPET II: design, development, and initial performance of an improved microPET scanner for small-animal imaging *Phys. Med. Biol.* **48** 1519–37

Watanabe M, Okada H, Shimizu K, Omura T, Yoshikawa E, Kosugi T, Mori S and Yamashita T 1997 A high resolution animal PET scanner using compact PS-PMT detectors *IEEE Trans. Nucl. Sci.* **44** 1277–82

Weber S, Terstegge A, Herzog H, Reinartz R, Reinhart P, Rongen F, Muller -Gartner H W and Halling H 1997 The design of an animal PET: flexible geometry for achieving optimal spatial resolution or high sensitivity *IEEE Trans. Med. Imaging* **16** 684–9

Yavuz M and Fessler J A 1998 Statistical image reconstruction methods for randoms-precorrected PET scans *Med. Imaging Anal.* **2** 369-78369-78

Yoshizawa Y, Ohtsu H, Ota N, Watanabe T and Takeuchi J 1997 The development and the study of R5900-00-M64 for scintillating/optical fiber readout 1997 *IEEE Nuclear Science Symposium Conference Record* vol 1 (Piscataway, NJ: IEEE) pp 877–81

Ziegler S I, Pichler B J, Boening G, Rafecas M, Pimpl W, Lorenz E, Schmitz N and Schwaiger M 2001 A prototype high-resolution animal positron tomograph with avalanche photodiode arrays and LSO crystals *Eur. J. Nucl. Med.* **28** 136–43